All-Optical Multimodal Mapping of Single Cell Type-Specific Metabolic Activities via REDCAT

Yajuan Li[1#], Zhaojun Zhang[2#], Archibald Enninful[3#], Jungmin Nam[3], Xiaoyu Qin[3], Jorge Villazon[1], Negin Fazard[3], Anthony A. Fung[3], Mina L. Xu[4], Hongje Jang[1], Nancy R. Zhang[2], Rong Fan[3,5,6]*, Zongming Ma[7]*, Lingyan Shi[1]*

[1]Shu Chien-Gene Lay Department of Bioengineering, University of California, San Diego, La Jolla, CA, USA.
[2]Department of Statistics and Data Science, The Wharton School, University of Pennsylvania, Philadelphia, PA, USA.
[3]Department of Biomedical Engineering, Yale University, New Haven, CT, 06520, USA.
[4]Department of Pathology, Yale School of Medicine, New Haven, CT, 06520, USA.
[5]Yale Stem Cell Center and Yale Cancer Center, Yale School of Medicine, New Haven, CT, 06520, USA.
[6]Human and Translational Immunology Program, Yale School of Medicine, New Haven, CT, 06520, USA.
[7]Department of Statistics and Data Science, Yale University, New Haven, CT, 06520, USA.

*Co-correspondence: R. F. rong.fan@yale.edu, Z. M. zongming.ma@yale.edu, L. S. l2shi@ucsd.edu
Lead contact: l2shi@ucsd.edu

Abstract

Metabolism dictates a range of physiological functions in human health and disease. Metabolic activities vary substantially in different cell types and are influenced by local tissue environments. Despite latest advent in spatial omics to map cellular heterogeneity and neighborhoods, it is yet to connect cell type or state to metabolic function, ideally, cell-by-cell in same tissue section to unveil metabolic mechanisms in a cell-type-specific manner in complex tissue. Here we present Raman Enhanced Delineation of Cell Atlases in Tissues (REDCAT) for spatially co-profiling metabolic activities and cell types via integration of all-optical multi-modal chemical imaging with high-plex immunofluorescence imaging on the same tissue section. Application to human normal and malignant lymphoid tissues maps metabolic processes including protein, nucleic acid, and lipid metabolism as well as intra-cellular lipid droplet (LD) diversity to all cell types and unveils metabolic reprogramming in lymphoma development and progression. Hyperspectral imaging further revealed subcellular chemical composition changes in individual cancer cells. REDCAT enables the mapping of single-cell type-specific metabolic activities in complex tissues to explore the landscape of cellular phenotype–function relationship, providing rich biological information potentially for clinical pathology and disease diagnosis.

Keywords:
optical imaging, SRS, immunofluorescence, metabolism, lymph node, lymphoma, lipid droplet

Introduction

Metabolism regulates cell function in normal physiology and disease such as cancer and immune response[1,2]. Metabolic state, a balance between energetic and biosynthetic pathway [2,3], is determined by intrinsic and extrinsic signaling. Characterizing the metabolic state of individual cells is fundamental to improving our understanding of complex biological systems. However, little is known about how cell metabolism is altered in individual cells in complex tissues in response to cell-cell interactions and inter-cellular signaling due in part to the lack of spatially resolved measurement of single cell metabolism and phenotype in situ directly in complex tissues. Despite the latest development in spatial transcriptomics [4-7] and proteomics [7-10] that transformed the study of single-cell heterogeneity and neighborhoods in tissue, it is yet to incorporate metabolomic information to link metabolism to cell type.

Recent technological advancements in mass spectrometry imaging (MSI) including matrix-assisted laser desorption/ionization (MALDI), desorption electrospray ionization (DESI), and secondary ion mass spectrometry (SIMS), have allowed spatial profiling of a large number of proteins and metabolites. Integrated with multiplexed protein markers, these approaches possess the capability to characterize metabolic heterogeneity with distinct sensitivity, spatial resolution, and chemical coverage. For example, a recent fluorescence imaging conjugated MALDI metabolic mapping method named SapceM [11] was employed to map out the metabolic profiles in single cultured cells, but it has limited resolution to measure metabolic processes of single cells in compact tissue samples. Spatially resolved metabolomic profiling built on TOF-SIMS measurements such as 3D-SMF [12] and scSpaMet [13] have achieved cell type-specific protein and metabolite analysis in tissues. However, most of these methods are inherently destructive, difficult to adopt in cell biology or tissue histopathology labs, or do not reach the subcellular organelle resolution, not to mention the challenge in metabolite annotation. Raman spectroscopy provides a non-destructive and label-free method to quantitatively analyze biomolecules in cells and tissues. It works by fingerprinting the energy shift of scattered photons elicited by the changes in chemical bond vibrational modes within the biomolecules such as nucleic acids, proteins, and lipid metabolites, upon interaction with light, at subcellular spatial resolution [14-16].

Abnormal lipid metabolism is associated with various diseases linked to lipodystrophy, oxidative stress, insulin resistance and inflammation, such as metabolic syndrome, infections, cancer, and neurodegeneration [17,18]. The function of lipids is to provide energy and building blocks for metabolic processes and membrane biosynthesis [17,18]. Lipid droplets (LDs) are intracellular organelles critical for lipid storage and metabolism [18,19]. They consist of a mono-phospholipid layer embedded with distinct proteins and a core containing neutral lipids such as triacylglycerols and sterol esters [19]. Accumulating evidence shows that LDs prevent cells from lipotoxicity and reactive oxidative species (ROS) damage via sequestering polyunsaturated fatty acids (PUFAs) [20]. Moreover, LDs are being appreciated as signaling hubs that integrate metabolism and inflammation [21]. LDs vary substantially in composition [22-24], which is implicated in metabolic heterogeneity. The LD diversity cannot be resolved by lipophilic stains such as BODIPY but can be well quantified by *in situ* Raman hyperspectral imaging [24].

Nicotinamide adenine dinucleotide (NADH) and flavin adenine dinucleotide (FAD) are metabolic cofactors participating in a wide range of cellular oxidation-reduction reactions including glycolysis and oxidative phosphorylation [25]. Two-photon excitation fluorescence (TPEF) imaging of the endogenous NADH and FAD offers another non-destructive and label-free way for assessing cell metabolism and redox status [26]. The radiometric imaging of NADH/ FAD can be used to quantitatively measure cell redox state [27,28]. The increase in this ratio of a cell can be interpreted as a relatively higher rate of glucose catabolism to oxidative phosphorylation, and vice versa [27,28].

To analyze metabolic state of heterogeneous cell types in tissue at subcellular level, we propose Raman Enhanced Delineation of Cell Atlases in Tissues (REDCAT), an integrative technology framework for profiling cell type-specific metabolic activities by incorporating Raman probed metabolomics and high-plex protein-based cell tying in a single pipeline. REDCAT combines label-free multimodule stimulated Raman scattering (SRS) imaging that achieves submicron resolution for *in situ* measurement of metabolites and redox status with high-plex protein imaging via co-detection by indexing (CODEX) for cell typing in the same tissue section. Images from these two modalities are registered with high precision and then correlated extraction of single-cell features, including metabolic and protein signatures, is subsequently used for downstream clustering, annotation of distinct cell types, and cell type-specific metabolic processes. We demonstrated systematic analysis of metabolic redox, lipid

metabolism and LD heterogeneity in individual cells and different cell types as determined by protein marker, all done in the same tissue section to derive a spatial atlas of single-cell type-specific metabolic state.

Design and Workflow of REDCAT

REDCAT directly links single-cell protein profiles to the metabolism data on the same tissue slide. In order to understand the tissue histology for subsequent REDCAT analysis, one of the serial sections (10μm thick) prepared from a Formalin-Fixed Paraffin-Embedded (FFPE) tissue block is stained for Hematoxylin and Eosin (H&E). An adjacent tissue section is subjected to REDCAT by firstly performing the label-free metabolic profiling using two-photon excitation fluorescence-stimulated Raman scattering (TPEF-SRS) microscopy. At the single cell level, NADH and FAD were measured from TPEF autofluorescence while unsaturated lipids, saturated lipids, and total lipids were simultaneously acquired at the same region of interest (ROI) by label-free SRS imaging with Raman shifts 2930 cm^{-1}, 3015 cm^{-1}, 2880 cm^{-1} and 2850 cm^{-1}, respectively. Endogenous fluorescence ratio NADH/FAD is used to access cell metabolic redox [29]. The Raman intensity ratio calculated by 2850 cm^{-1}/3150 cm^{-1} indicates relative lipid abundance. The ratio 3015 cm^{-1}/2880 cm^{-1} indicates the level of lipid unsaturation, which is correlated with membrane fluidity and oxidative stresses [30]. To further profile the detailed chemical properties of *in situ* metabolites, hyperspectral images within a Raman spectral range 2700-3150 cm^{-1} were acquired with 51 dimensions at a submicron resolution. Lastly, the same tissue section is subsequently imaged with high-plex protein immunofluorescence via CODEX to identify all major cell types. In this work, we applied a panel of 40 protein markers and imaged with 0.5μm per pixel resolution. After all the imaging procedures, the sequential TPEF-SRS and CODEX datasets were co-registered to the single cell level, where the spatial maps of subcellular metabolic activity and lipid profile in each cell were extracted, correlated with protein-defined cell types, and then subjected to the downstream quantitative analysis (Figure 1).

The REDCAT imaging pipeline incorporated sequential detection of metabolic and proteomic information within the same tissue. Single-cell features from both modalities are extracted following cell segmentation, with cell boundaries identified using pretrained Mesmer models. Affine transformations are applied for spatial alignment, precisely registering CODEX and SRS images at the cellular level to ensure correspondence between molecular features and metabolic features. This cross-modality integration enables REDCAT to provide *in situ* metabolic activity and lipid profile information at single-cell resolution, directly connecting between protein expression and cell typing to the metabolic state such as those defined by the biochemical ratios such as NADH/FAD, Lipid/Protein, and Unsaturated Lipid/Saturated Lipid (Figure 1).

REDCAT maps immune cell type-specific metabolic states in normal human lymph nodes

Immune cells undergo dynamic processes such as proliferation, differentiation, activation, and response to extracellular signals or stressors. These processes are regulated by the orchestrated expression and function of multiple genes and accompanied by metabolic programming [31]. In order to understand immune cell dynamics in vaccine response or immunotherapies, it is essential to study metabolism in immune organs at single cell level.

Lymph nodes are part of the secondary lymphoid organs. They are primarily made up of B cells and T cells in coordination with dendritic cells, macrophages and other stromal cells around the lymphatic follicle regions [31,32]. Germinal centers (GC) are transient anatomical structures that provide a unique microenvironment for B-cell affinity maturation. Upon activation, naïve B cells in the germinal center (GC) rapidly proliferate in response to T cell-dependent antigens and undergo antibody affinity maturation. In this scenario, B cells rapidly alternate between distinct "metabolic states" across quiescence, proliferation, and differentiation. The GC is formed by two histologically distinct regions: the dark zone (DZ) consists of highly proliferative GC B cells and the light zone (LZ) where GC B cells are less dividing and undergo a series of selection processes to develop mature plasma B cells. It has been documented that the activation of B cells leads to higher oxygen consumption, enhanced glycolysis leading to increased production of lactate. This process also causes higher consumption of amino acids including alanine and glutamine used as carbon and energy sources [31,32]. LZ B cells are hypoxic due to the low amounts of oxygen in the GC microenvironment. Low-oxygen tension promotes a high glycolytic rate, leading to increased B-cell apoptosis, reduced proliferation, and support for the antigen-driven selection process [33]. More recent evidence suggested that highly proliferative DZ B cells are non-glycolytic, uptake fatty acids, and obtain energy from the fatty acid oxidation (FAO) pathway [34]. However, it remains unclear which GC B cells go through which metabolic processes and whether it is a heterogenous or homogenous process occurring in lymph nodes, requiring the methods

to directly visualize the metabolic states *in situ* across diverse cell types during GC reactions. We reasoned that dissecting the single-cell resolved metabolic redox and lipid profile changes in lymph nodes by TPEF-SRS imaging coupled with CODEX-based cell typing would be informative for understanding the metabolic regulation of the germinal center response at single cell level.

REDCAT was therefore applied to a normal FFPE human lymph node to characterize the protein-metabolic environment around lymphatic follicles (Figures 2A, 2D, S1A and S2A). Herein, TPEF-SRS images were co-registered with the CODEX image using an antibody panel of 47 protein markers that was utilized for cell segmentation and annotation. These markers included surface markers for immune cells, cytokine receptors, proliferation marker, and extracellular matrix proteins (Figure S1A). After cell segmentation and unsupervised clustering of single-cell protein profiles, we identified 9 distinct clusters, which are spatially organized in concordance with histological structures (Figures 2B, 2C and S2B). Specifically, these clusters correspond to the follicle zone (cluster 3, 4, 5, 6, 8), interfollicular zone (cluster 0, 1, 2, 7), germinal center (GC) light zone (LZ) (cluster 4, 6) and GC dark zone (DZ) (cluster 3).

The metabolic profile of each cluster was extracted and quantified, revealing a negative correlation between total lipid levels and redox ratio while a positive correlation between unsaturated lipid levels and redox ratio in most clusters. This relationship suggests higher lipid metabolic activities resulting in lower redox state (Figures 2D and 2E). Notably, cluster 4 (in yellow), which indicates B cells in the light zone have a higher redox ratio and unsaturated lipid ratio compared to cluster 3 (in blue), which contains DZ B cells. Similarly, a group of macrophages (cluster 8 in green) located near the GC light zone (Figure 2F) possesses a high redox ratio. These results together indicate that cells in the light zone might be experiencing a more reduced state and have more fluid cell membranes. We further annotated cells using CODEX marker expressions and evaluated the metabolic state of each cell type (Figures 2G, 2H, 2I, S2C and S2D). Inside the follicles, we found that various cell types in the light zone exhibit a higher redox ratio and greater lipid level, especially the unsaturated lipid level compared to those in the dark zone (Figures 2H, 2I and S2D). Outside the follicles, we observed an inverse correlation between the redox ratio and unsaturated lipid levels in dendritic cells and a subtype of CD8 T cells (Figures 2H, 2I, S2D and S2E). These cells exhibited a higher redox ratio but lower levels of unsaturated lipids and total lipids. It suggests these cells favor NADH-generating catabolic processes over lipid synthesis, which is dependent on cell types and spatial localization.

We then examined the metabolic profiles of individual CD68 expressing macrophages scattered in and out of follicles (Figures 2J and 2K). Macrophages were identified as large cells containing a smooth ovoid nucleus with a distinct nucleolus, and high numbers of granules and lysosomes found within their cytoplasm [35,36]. Intriguingly, SRS imaging shows these macrophages have a higher lipid level, but lower redox ratio compared with surrounding CD20 positive B cells, indicating active oxidative metabolism of fatty acids (Figures 2L, 2M, 2N, 2O and 2P). SRS hyperspectral imaging validated the high lipid level in macrophage cytoplasm (Figure 2Q). Prior reports showed the presence of increased lipids in heterolysosomes of macrophages [37] and these lysosome-localized lipids can be used for LD generation [38]. We posited that the lipids found in macrophage cytoplasm are mainly localized in LDs. To support this hypothesis, we performed super resolution SRS hyperspectral imaging specifically on the cellular LDs and found macrophage LDs contain high intensity of lipid Raman vibrational models 2850 cm^{-1} and 2880 cm^{-1}. Furthermore, LDs laden CD20 positive or INF-G positive cells were found in close proximity to macrophage, suggesting possible metabolite exchanges between these neighboring cell types (Figures 2R and 2S). However, the Raman hyperspectral imaging indicates CH vibration of cell type specific LDs were distinct from each other (Figures 2R and 2S). It indicated that LD diversity might be crucial for cell identity and immune function. Nonetheless, the signaling pathways regulating the lipid metabolism in each single cell type and their influence on GC reaction warrant further study. Notably, we found a substantial difference of LD level can be commonly detected in the same cell type as shown in (Figure 2R), indicating metabolic heterogeneity within the same cell population dependent on spatial location and differentiation state. For example, some CD20 positive B cells exhibited dramatic LD accumulation than others, which could be associated with different differentiation stages of B cells and further underscore the importance of spatial metabolic heterogeneity in the tissue context, where cells do not function in isolation but are influenced by spatial location and surroundings. Altogether, our results stress the unique capability for REDCAT to identify cell type specific metabolic status *in situ* in human tissues.

REDCAT investigates the cell type-specific metabolic states in lymphoma

Cancer cells undergoing rapid proliferation or progression may need to change their metabolic state to meet the increasing demand for energy and building blocks [39,40]. This leads to a shortage of critical nutrients and builds up a hypoxic and acidic tumor microenvironment (TME). These factors together result in lower activation and recruitment of anti-tumor effector immune cells [39]. To further highlight the utility of REDCAT to assess the differential metabolic states in both normal and malignant immune cells, we applied this approach to a human lymphoma tissue sample to uncover novel metabolic processes in individual cells that may shed light on for therapeutic intervention targeting metabolic perturbations (Figures 3A, 3B, 3C, S3A, S4A and S4B). This lymphoma sample is very unique in that it contains the region of chronic lymphocytic leukemia (CLL), a low-grade lymphoma, and transition to the region of diffuse large B-cell lymphoma (DLBCL), a process known as Richter's transformation.

High-plex immunofluorescence CODEX imaging and cell typing further confirmed this histopathological diagnosis. The H&E image showed the characteristics of small B cells (as observed in CLL) in the lower half of the lymphoma sample which transitions to a region of diffuse large B cells in the upper half of this sample (Figures 3B, S3A and S4A) (Figures 3A and S4B). The unsupervised clustering of 35 protein markers identified 12 distinct clusters (Figures 3D and 3E). With REDCAD, the metabolic profile of each cluster was analyzed and the reverse correlation between total lipid levels and redox ratio found in normal lymph nodes was not maintained in malignant lymph nodes. Furthermore, there was no obvious correlation between other metabolic features (Figure 3F), suggesting the profound departure from metabolic homeostasis in tumor cells and niches. Astir-based single cell annotation and metabolic data integration was exploited to analyze cell type specific metabolism (Figures 3G, 3H, 3I, 3J and S4C). The results showed the levels of global lipids and unsaturated lipids as well as redox ratio were higher in the CLL region compared to DLBCL region (Figures 3G, 3H, 3I and 3J). The dramatic change of metabolic activities between these two regions indicates that tumor B cells and their surroundings undergo metabolic reprogramming during transformation from indolent to aggressive lymphoma in order to adapt to the harsh conditions of the tumor microenvironment, such as hypoxia and nutrient deprivation. DLBCL cells are characterized by the high expression level of CD20 protein as compared to CLL cells (Figures 3C and S3A). Additionally, DLBCL cells are highly proliferative indicated by Ki67, which is a nuclear protein associated with cellular proliferation (Figures S3A and S4A). These cells have a large cell body, containing a large irregular nucleus equipped with small dense spherical nucleoli (Figures 3A, 3C, S3A and S4A). Prior study showed DLBCL cells exhibit high glucose uptake and enhanced glycolysis [41,42]. Consistently, we found the NADH/(NADH+FAD) ratio was increased in DLBCL cells compared to CLL cells as well as the non-malignant surrounding cells (Figures 3I and 3K).

In line with the previous study [43], we detected CLL cells exhibiting notable lipid accumulation (Figures 3B and 3K) in the cytoplasm. These excess lipids, which can be scavenged from their environment or *de novo* synthesized, are stored in lipid droplets. We further revealed that the reprogramming of lipid metabolism occurs in DLBCL cells during the transition from CLL (Figures 3B and 3K). Compared to the lipid cluster shown in CLL cells, DLBCL cells showed a higher lipid level in the cell membrane (Figure 3K), suggesting DLBCL may adapt their lipid metabolism to support rapid membrane growth and survival in a relatively less friendly microenvironment. Despite the increased number of CD68 positive macrophages in DLBCL compared to that of normal lymph nodes (Figs. S1A and S2A), we did not find a significant lipid accumulation in these cells as we found in the normal lymph node section (Figure S4D). It indicates metabolic remodeling potentially implicated in the conversion from classically activated M1 to alternatively activated M2 macrophage in the DLBCL microenvironment [44].

Collectively, REDCAT empowers us to spatially elucidate the metabolic transformation from low-grade to high-grade tumor at single cell level, enhancing our understanding of the metabolic reprogramming of heterogenous cell types in the lymphoma tumor microenvironment.

Hyperspectral REDCAT reveals single-cell lipid profile changes during human lymphoma transformation

To extend the cell specific lipid subtype analysis in tumor tissues, we performed SRS hyperspectral imaging from a region intermixed with large B and CLL tumor cells (Figures 4A, 4B, S5A and S6A). This sample shows a rarely captured pathology whereby the low-grade tumor is still seen in substantial spatial distribution adjacent to the transformed high-grade tumor, and the boundary is clearly defined, even as seen by light microscopy. The cell types were then delineated by CODEX markers. Consistent with the previous tumor ROI, the SRS-lipids signal was shown as tight clusters in the CLL region while scattered in the DLBCL region (Figures 4C and 4D). Notably, the

high-resolution SRS imaging enables us to visualize the subcellular distribution, structure and content of LDs in different cell types. In contast to the large LD size in CLL cells, the LD size is significantly reduced in DLBCL cells (Figure 4E). We further demonstrated each SRS hyperspectral clustering (Figures 4F and 4G), revealing unique metabolic variations spatially correlated with spatially distinct cell subpopulations determined by CODEX protein clustering (Figures 4C and 4H). Notably, the distribution of SRS cluster 6 (yellow) and cluster 8 (blue) cells were mainly colocalized with the CLL cells in CODEX cluster 1 (red). Consistently, DLBCL cells in CODEX cluster 6 (yellow) manifest in the Raman spectra cluster 1(magenta) and cluster 4 (sky blue). Interestingly, we found endothelial cells (green) in close proximity to CLL cells (red) gain a similar metabolic profile as CLL cells (Figure 4H). We posit that CLL cells release exosomes containing metabolites that are taken up by adjacent endothelial cells. These exosomes can reprogram endothelial cells to produce cytokines that support CLL cell survival and proliferation[44]. We observed that a subgroup of T cells (dark blue, codex cluster 0), dendritic cells (in sky blue, codex cluster 7), and macrophages (in black, codex cluster 3) accumulate more lipids than the main group in each cluster. They may represent cancer cells at different developmental stages (Figure H). This result suggests that SRS hyperspectral imaging can add another layer of information for classification of functional cell subtypes. Despite this common feature of lipid accumulation, these cells exhibit a distinct ratio between Raman spectra clusters from CLL and DLBCL cells (Figure 4H), indicating major cell type-specific metabolic profile. Notably, the cells in CODEX cluster 4 (magenta) are often found in close proximity to macrophages (black), suggesting that the spatial distribution of macrophages may play a role in lymphoma transformation. These cells in cluster 4 exhibit similar morphology to CLL but cannot be specifically identified by the protein markers. From SRS hyperspectral imaging, we noticed that these cells display a wide range of lipid levels from barely any lipids to heavily lipid accumulation (Figure H), indicating a highly dynamic and heterogenous metabolic profile, suggesting that this cluster might represent an intermediate or transient state of CLL transformation.

To capture the metabolic trajectory of transformation processes from CLL and DLBCL, we arbitrarily defined the cells located between CLL and DLBCL regions as adjacent CLL and DLBCL and compared their metabolic profiles to that of large B and CLL cells inside the CLL and DLBCL region, respectively (thereafter distal CLL and DLBCL) (Figure 4H). We found that adjacent CLL and DLBCL cells show a distinct metabolic profile from the distal CLL and DLBCL cells, especially lower levels of lipid accumulation (Figure 4H). This result further support the notion of a putative intermediate state that may exist during CLL to DLBCL transition, which was identified by label-free SRS imaging. In addition, CD4 T cells surrounding the distal CLL cells has higher level of lipid accumulation than the ones near adjacent CLL and DLBCL cells (Figure S7), indicating disturbed lipid homeostasis, which may impair the function and proliferative capacity of these CD4 T cells.

Interestingly, high-resolution single-cell SRS imaging uncovered a significant presence of lipids colocalized within the nucleoli of large B lymphoma cells that has not been reported previously (Figure 4I). This was validated by the high intensity of Raman vibration from lipid modes (Figure 4J). Previous study shows nucleolar protein RRP-8 suppression is linked to abnormal lipid accumulation in the *C. elegans* by inducing nucleolar stress [46]. Cytochemical and autoradiographic study evidences the presence of lipids in the nucleoli [47]. We hypothesize that nucleolar lipids might be involved in signaling pathways, regulating gene expression, and maintaining the structural integrity of the nucleolus during the large B tumor cell transformation. However, the exact function and mechanisms of their involvement are yet to be further studied. Meanwhile, we observed an upregulated level of membrane lipids found in the nuclear envelope of large B cells than the surrounding CD4 T cells (Figure 4I and 4K), indicating lipid reconstitution of nuclear envelope for nuclear envelope integrity [48]. Altogether, REDCAT combining hyperspectral SRS and CODEX further enables in-depth exploration of lipid metabolic processes in situ in highly heterogeneous cell populations in human tumor tissues. The REDCAT pipeline holds the potential for discovering new diagnostic markers and tracking the metabolic trajectory of cancer cells as they progress from low-grade to high-grade tumors, potentially for early detection of lymphoma transformation, patient stratification, and individualized treatment.

Discussion

We have developed REDCAT, a multimodal all-optical platform that seamlessly integrates SRS chemical imaging and high-plex CODEX immunofluorescence imaging to enable the spatial exploration of proteomics and metabolic activities at the single-cell level in complex tissues including clinical archival FFPE samples. This platform allows us to spatially profile single-cell redox status and lipid metabolites. REDCAT not only tracks metabolic

reprogramming during normal immune cell activation but also accurately delineates the metabolic features of tumor development and progression. Our study indicates that the important lipid species are still preserved in deparaffinized FFPE tissues, likely due to the compact cellular structure that retains small molecules during formalin fixation. Although such samples may not well suited for high coverage mass spec lipidomics, SRS allows for *in situ* imaging of major lipid metabolic processes such as lipid unsaturation, accumulation, LD formation, and spatial location. The capability of REDCAT to spatially explore lipid biology in FFPE tissues holds transformative potential for clinical histopathology research.

In normal lymph node tissue, we observed that high lipid levels are negatively correlated with the NADH/(NADH+FAD) ratio. This finding led us to hypothesize that lipid metabolic activity together with redox ratio could be used to determine the metabolic homeostatic state of immune cells in human lymph nodes. However, this correlation is disrupted in malignant lymphoid tissues such as in CLL and DLBCL cells. In these tumor cells, both the global lipid levels and the redox ratio are upregulated, indicating significant metabolic remodeling. One possible explanation is that tumor cells are actively engaging in catabolism to generate NADH coping with the hypoxic stresses while simultaneously synthesizing lipid materials for cellular building blocks.

We observed that the transformation from CLL to DLBCL is accompanied by significant remodeling of lipid distribution, including nuclear and membrane lipids. DLBCL is often associated with chronic inflammation, which can be driven by a persistent inflammatory environment or Epstein-Barr virus (EBV) infection. In fact, this sample was clinically assessed for EBV and the large, transformed B cells were EBV positive. In sites of chronic inflammation, B cells can acquire genetic changes that promote lipid metabolic reprogramming, which primes tumorigenesis. While this study is exploratory and must be validated by additional focused cohorts, our findings may suggest a potential avenue for targeting abnormal metabolic processes to prevent tumor progression.

CLL and surrounding cell types such as CD4 positive helper T cells exhibit enriched lipid levels, suggesting that pathways involved in intercellular communication, metabolic modulation, and intracellular responses are also affected in the T cell compartment, thereby leadings to impaired anti-tumor T cell immunity or creating a potentially tumor-promoting immune environment. The accumulation of lipids may result from the upregulation of lipid synthesis and the downregulation of lipogenesis. These lipids can originate from *de novo* lipogenesis or be scavenged from the environment. In CLL, CD36 protein expression, which mediates lipid uptake, increased significantly in accordance with the lipid metabolism upregulation observed by SRS. Additionally, lysosome abundance is reported to be higher in CLL, potentially participating in the lipid processing through autophagy. These lipids can serve as the energy source and building blocks for rapid proliferation [43]. Alternatively, toxic lipids, such as oxidative lipids from membranes or external sources, can be sequestered in lipid droplets (LDs), protecting cells from lipotoxicity. However, the metabolic routes of these lipids need further validation. Combining isotope-probed SRS imaging [14] with genome-wide spatial omics profiling such as Patho-DBiT [49] to explore specific lipid metabolism genes in different cell type and transcriptional state can help decipher the source of the lipids and the mechanisms regulating LD generation in normal physiology or tumorigenesis.

Beyond the abnormal excess lipid storage, other cell types in the tumor environment may exhibit lipodystrophy. In normal macrophages, lipids detected in CD68-positive vesicles are likely derived from debris of endocytosed cells, indicating active macrophage function in maintaining immune surveillance. However, in infiltrated macrophages of DLBCL, lipid levels were reduced, suggesting a dysfunction in processing endocytosed cell debris and a compromised metabolic flux through lysosomes. Altogether, investigating why, when, and how lipid metabolism correlates with metabolic features across various cell types in tumor niche is essential for a deeper understanding of tumor pathology and REDCAT provides a valuable tool to map metabolic mechanisms in single-cell type-specific in complex biological systems including clinical tissue specimens.

Materials and methods

Tissue specimens

De-identified archived formalin-fixed paraffin-embedded (FFPE) human reactive lymph node and lymphoma tissue samples were obtained from Yale Pathology Tissue Services (YPTS). The retrieval and distribution of these tissues for research purposes were approved by the Yale University Institutional Review Board and overseen by the Tissue

Resource Oversight Committee. In cases where identifiable information was associated with the specimens, written informed consent was obtained from the patients or their guardians, in accordance with the Declaration of Helsinki. All samples were processed in strict adherence to HIPAA regulations, University Research Policies, Pathology Department diagnostic protocols, and Hospital by-laws.

Human tissue section preparation

After review of all slides by board-certified pathologist and selection of the optimal block, paraffin blocks were sectioned at a thickness of 7-10 μm and mounted on the center of Poly-L-Lysine coated 1 x 3" glass slides. Serial tissue sections were collected simultaneously for SRS, CODEX and H&E staining. The sectioning was carried out by YPTS and stored at −80°C until use.

Tissue deparaffinization and decrosslinking

The FFPE tissue sections were shipped to Dr. Lingyan Shi's Lab at UCSD for the SRS workflow. The tissue slides were bathed with fresh xylene for 5 min and then were transferred to fresh absolute ethanol for 5 min. Followed by incubating 95%, 75%, 50%, and 25% ethanol for 3 min sequentially, the slides were subjected to distilled water for 3 min to be fully hydrated.

SRS imaging and high-resolution imaging processing

The SRS images were collected from an upright laser-scanning microscope (DIY multiphoton, Olympus), which was equipped with a 25x water objective (XLPLN, WMP2, 1.05 NA, Olympus). The synchronized pulsed pump beam (tunable 720–990 nm wavelength, 5–6 ps pulse width, and 80 MHz repetition rate) and stokes beam (wavelength at 1031nm, 6 ps pulse width, and 80 MHz repetition rate) from a picoEmerald system (Applied Physics & Electronics) were coupled and introduced into the microscope. Upon interacting with the samples, the transmitted signal from the pump and Stokes beams was collected by a high NA oil condenser (1.4 NA). A shortpass filter (950 nm, Thorlabs) was used to completely block the Stokes beam and transmit the pump beam only onto a Si photodiode array for detecting the stimulated Raman loss signal. The output current from the photodiode array was terminated, filtered, and demodulated by a lock-in amplifier at 20 MHz. The demodulated signal was fed into the FV3000 software module FV-OSR (Olympus) to form images using laser scanning. SRS protein, lipid, unsaturated lipid and saturated lipid signal were obtained at vibrational modes 2930 cm^{-1}, 2850 cm^{-1}, 2880 cm^{-1} and 3015 cm^{-1} in a single tile of 512 x 512 pixels, at dwell time 40 μs and 100 tiles were stitched to generate the large tissue mapping. To quantify the unsaturated lipid ratio, the intensity of C=C vibrational modes (peak intensity at 3015 cm^{-1}) was divided by the intensity of saturated vibrational modes (peak intensity at 2880 cm^{-1}), resulting in ratiometric images. Minor intensity adjustment (brightness and/or contrast) was performed in ImageJ. The figures were assembled in Adobe Illustrator 2023. To reach a high resolution of the subcellular organelles, the measured images can be processed by Adam based Poinitillism Deconvolution (A-PoD). Based on a function to describe blurring pattern of point emitters, so called point spread function, the super-resolution images can be reconstructed [15].

SRS hyperspectral imaging and clustering analysis

SRS-hyperspectral images were collected from the same setup described above. The hyperspectral imaging stacks of LDs and membranes were taken with 51 spectral steps at 40 μs pixel dwell time, covering the whole CH stretching region from 2800 to 3150 cm^{-1}. The intensity profiles of the hyperspectral stacks from the regions of interest were plotted in ImageJ and further processed by baseline correction, smoothing and normalization in OriginPro 2017. Unsupervised K-means clustering method was applied to generate metabolic mapping at each pixel.

Optical redox imaging

The two-photon fluorescent microscopy was used to collect the NADH and FAD signals from the tissue. The NADH signal was excited by 780 nm, the emission wavelength was collected at 460 nm. The FAD signal was excited by 860 nm, the emission wavelength was collected at 515 nm. The ratiometric images were generated by FAD/NADH. The ratio was further quantified in ImageJ and plotted in GraphPad 10.

CODEX spatial phenotyping using PhenoCycler-Fusion

After receiving the slides following the SRS workflow, a modified version of the CODEX PhenoCycler-Fusion protocol (Link to protocol) was adopted. Since the tissue had already been deparaffinized and rehydrated during the SRS workflow, the CODEX process began with a gentle antigen retrieval step using 1X AR9 buffer for 5-10 minutes. The tissue was then allowed to cool to room temperature and was rinsed twice with nuclease-free water and hydration buffer, followed by staining buffer as the antibody cocktail was prepared. The tissue slide was incubated with the antibody cocktail at room temperature for 3 hours in a humidity chamber. After incubation, the tissue underwent a series of steps including post-fixation, ice-cold methanol incubation, and a final fixation step. Attached to the flow cell, the tissue section was incubated in 1X PhenoCycler buffer with additive for at least 10 minutes to improve adhesion. The CODEX cycles were then set up, the reporter plate was prepared and loaded, and the imaging process began. A final qptiff file was generated, at the end which could be viewed using QuPath V0.5.168. For further details on the PhenoCycler antibody panels, experimental cycle design, and reporter plate volumes, see Table - Codex panel details.

Flow cell removal and H&E staining

Following the CODEX imaging workflow, the flow cell can be removed, and histological H&E staining performed on the same tissue section. To remove the flow cell, the tissue slide with the flow cell is immersed in xylene or HistoClear for a minimum of 20 minutes to weaken the adhesive. A razor was then used to carefully detach the flow cell from the tissue slide. The tissue slide was then rinsed thoroughly with deionized water and then with 1X PhenoCycler Buffer without additive three times for 10 minutes each. Histological H&E staining on the FFPE sections was conducted by YPTS.

Preprocessing of CODEX data

Cell segmentation was performed using a StarDist-based model [50] in QuPath [51]. The DAPI channel served as the nuclear marker for cell segmentation. The mean intensity of each marker per segmented cell was exported together with the centroids of each cell as a CSV. Downstream analysis was performed using Seurat 4.3.0 package. The dataset was normalized and scaled using the NormalizeData and ScaleData functions. Linear dimensionality reduction was then performed with the "RunPCA" function. The "FindNeighbors" function embedded spots into a K-nearest neighbor graph structure based on Euclidean distance in PCA space, and the "FindClusters" function was used to cluster the spots. The "RunUMAP" function was used to visually show spatial heterogeneities through the Uniform Manifold Approximation and Projection (UMAP) algorithm. The clusters were plotted spatially using the ImageDimPlot function. The FindAllMarkers function was used to find the differentially expressed proteins in each cluster and the heatmap plotted using the DoHeatMap function.

Quality control and preprocessing for single cell analysis

Cell and nuclei boundaries were generated using the Mesmer [52] with pretrained weights. The DAPI channel was employed to identify nuclei, while the CD45 channel marked the cell membranes. The default resolution of 0.5 micro meters per spot was used for cell mask prediction. Only cells with sizes falling within the [0.05, 0.95] quantile range and exhibiting DAPI intensities above the 0.1 quantile threshold were included in the analysis. CODEX feature extraction involved summing the signal for each feature across individual cells. For each feature, the 0.05 and 0.95 quantiles were computed, and the values were normalized to fit within a [0, 1] scale, where 0 corresponded to the 0.05 quantile and 1 to the 0.95 quantile. Values outside this range were capped at 0 or 1, as needed.

Cell type annotation

Cell type annotation was performed using the Astir package [53]. Cleaned and normalized protein expression matrices were used as input, ensuring high-quality data for downstream analysis. Marker genes used in annotation included B cells (CD45, CD20, CD21), CD4+ T cells (CD45, CD3e, CD4), CD8+ T cells (CD45, CD3e, CD8), NK cells (CD45, CD107a), macrophages (CD45, CD68, CD163), monocytes (CD45, CD14), dendritic cells (CD45, CD141), and endothelial cells (CD31). The annotation process was initialized with the fit_state() function, using default parameters to estimate an initial probabilistic state for each cell. The fit() function was then applied to train the

model, which estimates the posterior probability of each cell belonging to predefined cell types based on marker expression patterns. Cells were annotated with the type showing the highest posterior probability.

SRS single cell analysis

To align a CODEX image with an SRS image, affine transformations were applied. Key control points were manually selected on both images and recorded as coordinate arrays. An affine transformation matrix was computed using skimage.transform.estimate_transform() based on these points. The SRS image was transformed with skimage.transform.warp() by applying the inverse of the estimated matrix to align it with the CODEX image. With the cell positions from both images, the learned transformation was used to register the cells, ensuring precise alignment of cellular-level data across the two modalities for other comparisons. Next, single-cell level ratios, including NADH/Flavin, Lipid/Protein, and Unsaturated Lipid/Saturated Lipid, were calculated. For each ratio, the 0.8 quantile was computed to capture high-value distributions. Scatter plots were generated to visualize the spatial distribution of the computed ratios across the tissue.

ACKNOWLEDGMENTS

We acknowledge the support received from the U.S. National Institutes of Health (NIH) including grants NIH R01GM149976, U01AI167892, 5R01NS111039, R21NS125395, U54DK134301, U54HL165443 (all to L. S.), U54CA274509, UH3CA257393, RF1MH128876, U54AG079759, U54AG076043, R01CA245313, RM1MH132648 (all to R.F.). and U01CA294514 (to R.F., M.X., and Z.M.). Dr. Lingyan Shi (L.S.) is a Sloan Research Fellow. Z.M. is supported by NSF awards 2345215 and 2245575. We also thank Yale West Campus cleanroom team for assistance with microfluidic wafer fabrications and the YPTS team for FFPE tissue sectioning and staining. Computational data analysis was conducted with the support of Yale High Performance Computing clusters (HPC).

Author Contributions

Conceptualization: L.S. and R.F.; Methodology: Y. L., Z. Z., A. E., R. F., Z. M. and L. S.; Experimental Investigation: Y. L., A. E., J. N., X. Q. and N. F.; Data Analysis: Y. L., Z. Z., A. E., J. V., A. A. F. and H. J.; Data Interpretation: M. L. X., R. F.,L. S. and Z. M.; Resources and valuable inputs: Y. L., A. E., Z. Z., M. L. X., N. F., J. N., X. Q. and N. Z. Original Draft: Y.L., A.E., Z.Z. All authors reviewed, edited, and approved the manuscript.

Competing interests

R.F. is scientific founder and adviser for IsoPlexis, Singleron Biotechnologies, and AtlasXomics. The interests of R.F. were reviewed and managed by Yale University Provost's Office in accordance with the University's conflict of interest policies. M.L.X. has served as consultant for Treeline Biosciences, Pure Marrow, and Seattle Genetics.

Main Figures and Captions

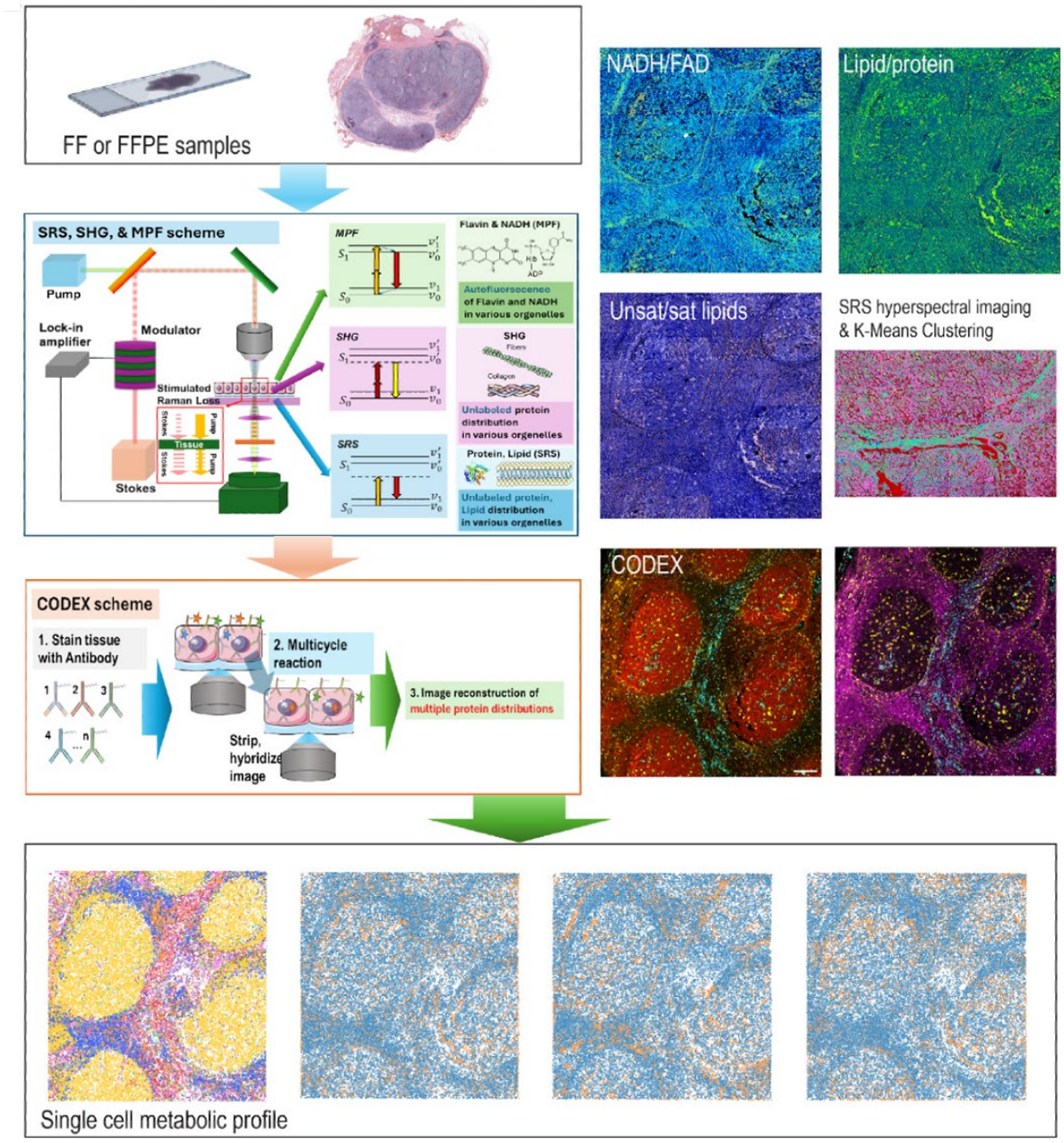

Figure 1. REDCAT workflow. A fresh or formaldehyde-fixed tissue slide is used as the starting material, which is imaged by a multimodal SRS imaging system that generates redox ratio, lipid ratio, and unsaturated lipid ratio as well as hyperspectral data of each pixel. Then, CODEX is implemented on the same piece of tissue recognizing a panel of proteins of interest. Afterward, computational analysis is performed to decipher the single-cell metabolic profile.

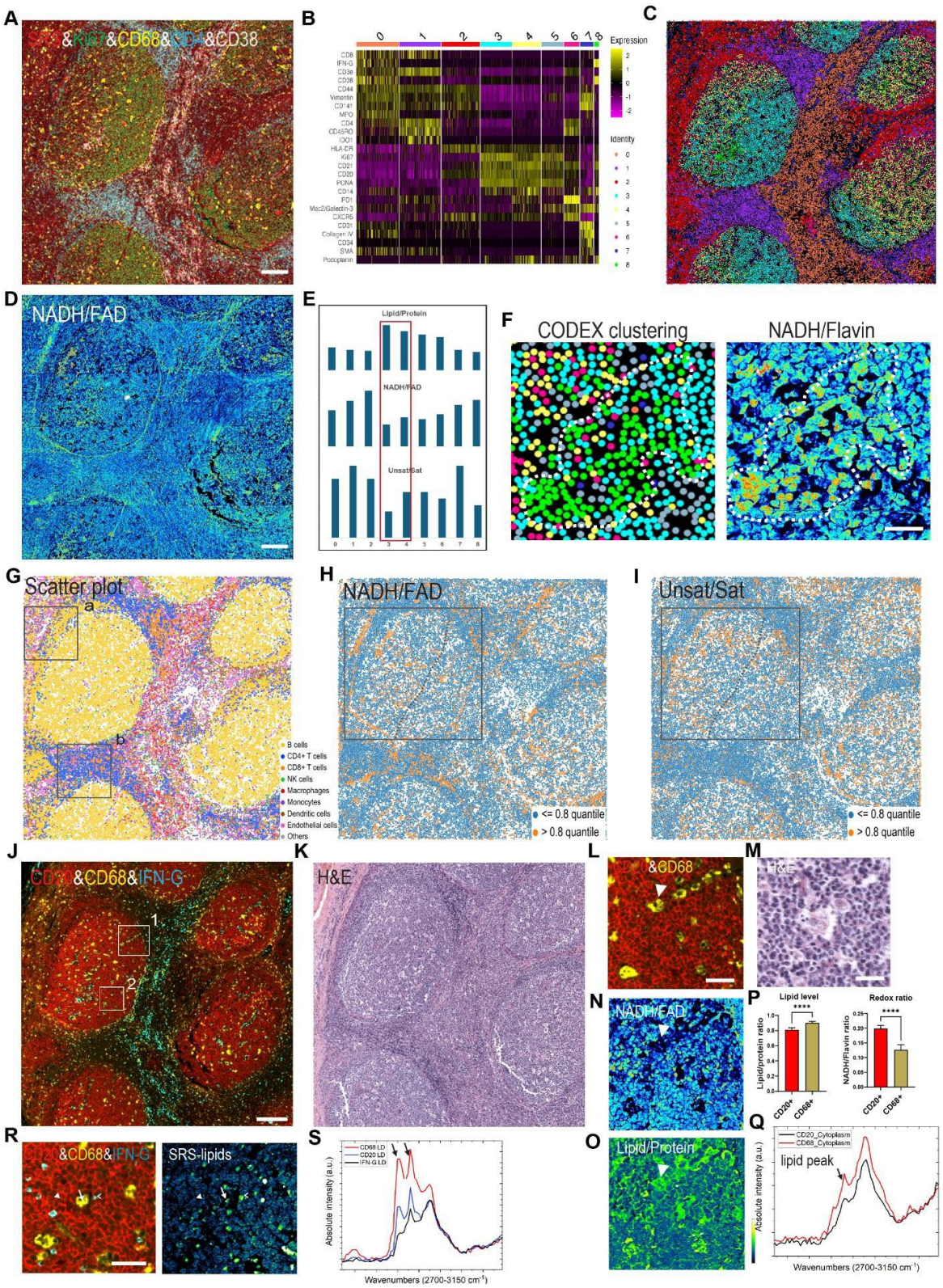

Figure 2. REDCAT profiles the metabolic state in a normal lymph node tissue. (A) An example to show TPEF-SRS is co-registered CODEX images on the same region of interest of normal lymph nodes showing cell specific endogenous metabolite distribution. Scale bar: 200 µm. **(B-C)** Unsupervised clustering of all the pixel-based protein expression profiles identified 9 distinct clusters in the normal lymph nodes. **(D)** Ratiometric image generated by two photon fluorescence imaging showing the mapping of redox state in normal lymph nodes.

Scale bar: 200 µm. **(E)** The redox, total lipid and unsaturated lipid ratio were extracted and quantified based on the CODEX clusters. The red boxed bars highlighted the metabolic comparison between cluster 3 (B cells in dark zone) and cluster 4 (B cells in light zone). **(F)** Side by side comparison of CODEX cluster 8 and its redox ratio. Scale bar: 50 µm. **(G)** Cell type annotation of CODEX dataset using Astir. The boxed areas were indicated in Figure S2E. **(H-I)** Scatter plots showing single cell redox ratio (indicated by NADH/Flavin) and unsaturated lipid level. The ROI inside the black box indicates a typical follicle with light zone and dark zone, which are separated by a dashed line. ROI 1 and 2 represent regions identified for further detailed analysis. **(J)** CODEX images identifying CD20, CD68 and IFN-G positive cells. The boxed ROIs indicated Figure 2L and 2R, respectively. Scale bar: 200 µm. **(K)** H&E image showing the histology of the region of interest in (J). **(L)** Zoomed in CODEX images with cell type markers of ROI 1 shown in (J). The arrowhead indicated a macrophage shown in (M). Scale bar: 20 µm. **(M)** H&E image showing the morphology of CD68 macrophage indicated by the arrowhead in (L). Scale bar: 10 µm.
(N) Two-photon excited fluorescent radiometric images generated by NADH/FAD mapping the cell specific redox state in ROI 1 shown in (J). **(O)** SRS radiometric images generated by 2850 cm^{-1}/2930 cm^{-1} (lipid/protein) mapping the distribution of lipids in the ROI 1 shown in (J). **(P)** Quantification of lipid level and redox state in the indicated cell types shown in (N) and (O). Data are presented as Mean ± SEM.
(Q) SRS hyperspectral imaging showing the spectral difference of cytoplasm between CD20 and CD68 cells. A typical lipid Raman peaks at 2880 cm^{-1} is indicated by the arrow. **(R)** Zoomed in CODEX and SRS images indicating cell type specific lipid droplet distribution of ROI 2 shown in (J). Scale bar: 20 µm. **(S)** SRS hyperspectral imaging delineates the spectral difference of lipid droplets in CD20 (triangle arrowhead), CD68 (arrow) and IFN-G (empty arrowhead) cells. The typical lipid Raman peaks at 2850 cm^{-1} and 2880 cm^{-1} are indicated by arrows.

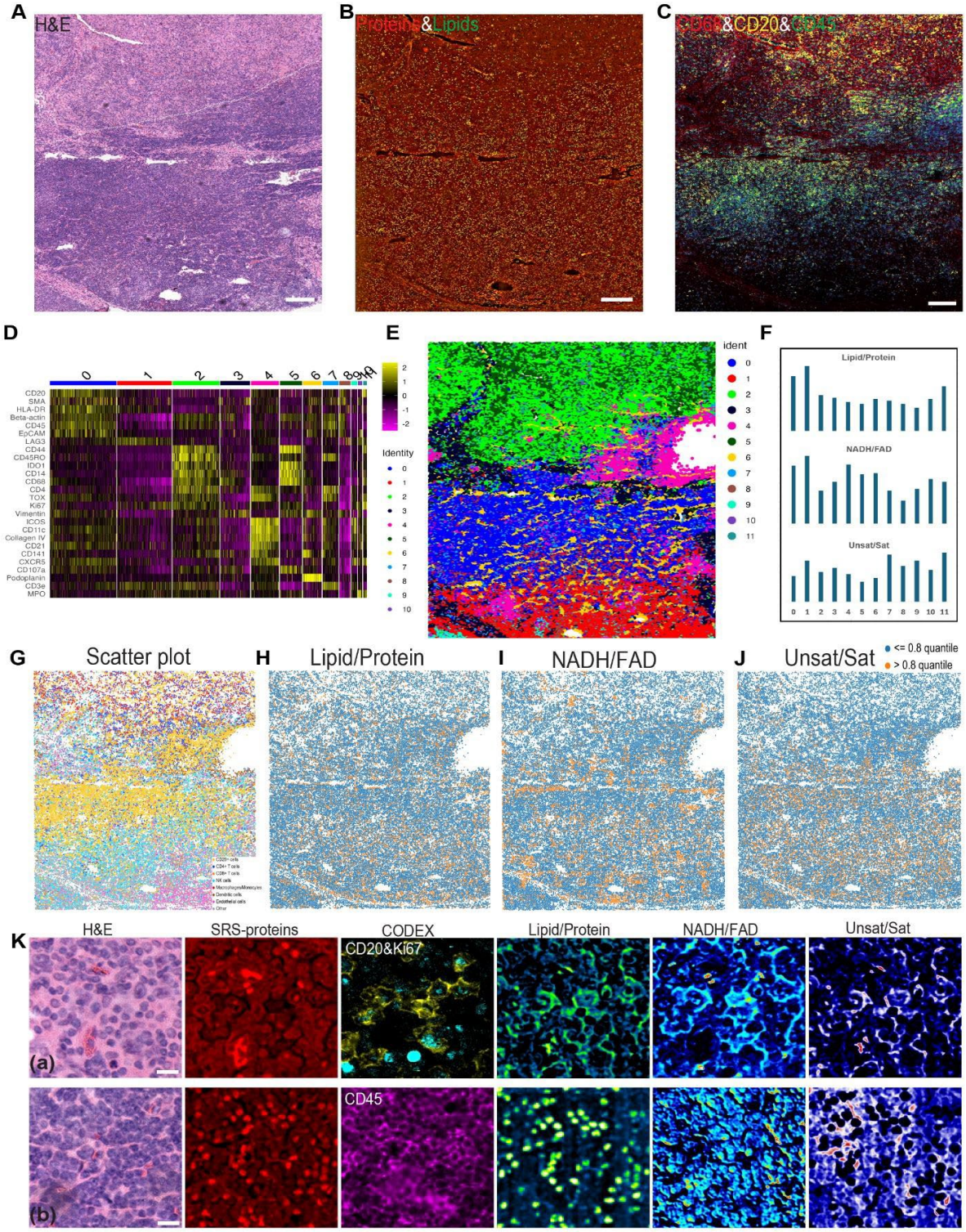

Figure 3. REDCAT profiles the metabolic state in a lymphoma tissue. (A) H&E image of the lymphoma showing the histology of the region of interest on which REDCAT was performed. Small B cells (as observed in CLL) in the bottom half transition to a region of diffuse large B cells in the top half in the H&E image. The dashed line roughly separated CLL and DLBCL regions. Scale bar: 200 µm. **(B)**

Overlapping SRS image showing the distribution of proteins and lipids in the lymphoma tissue. **(C)** Selected CODEX markers showing the distribution of CD68, CD20 and CD45 positive cells in the lymphoma tissue. **(D-E)** Unsupervised clustering of all the pixel-based protein expression profiles identified 12 distinct clusters in the lymphoma tissue. **(F)** The redox, total lipid and unsaturated lipid ratio were extracted and quantified based on the CODEX clusters in the lymphoma tissue. **(G)** The scatter plot shows the cell type annotations in the lymphoma tissue. **(H-J)** Scatter plots showing single cell lipid level (H), redox ratio (I) and unsaturated lipid level (J). **(K)** Side by side comparison of lipid and redox ratio distribution between DLBCL (a) and CLL (b) cells.

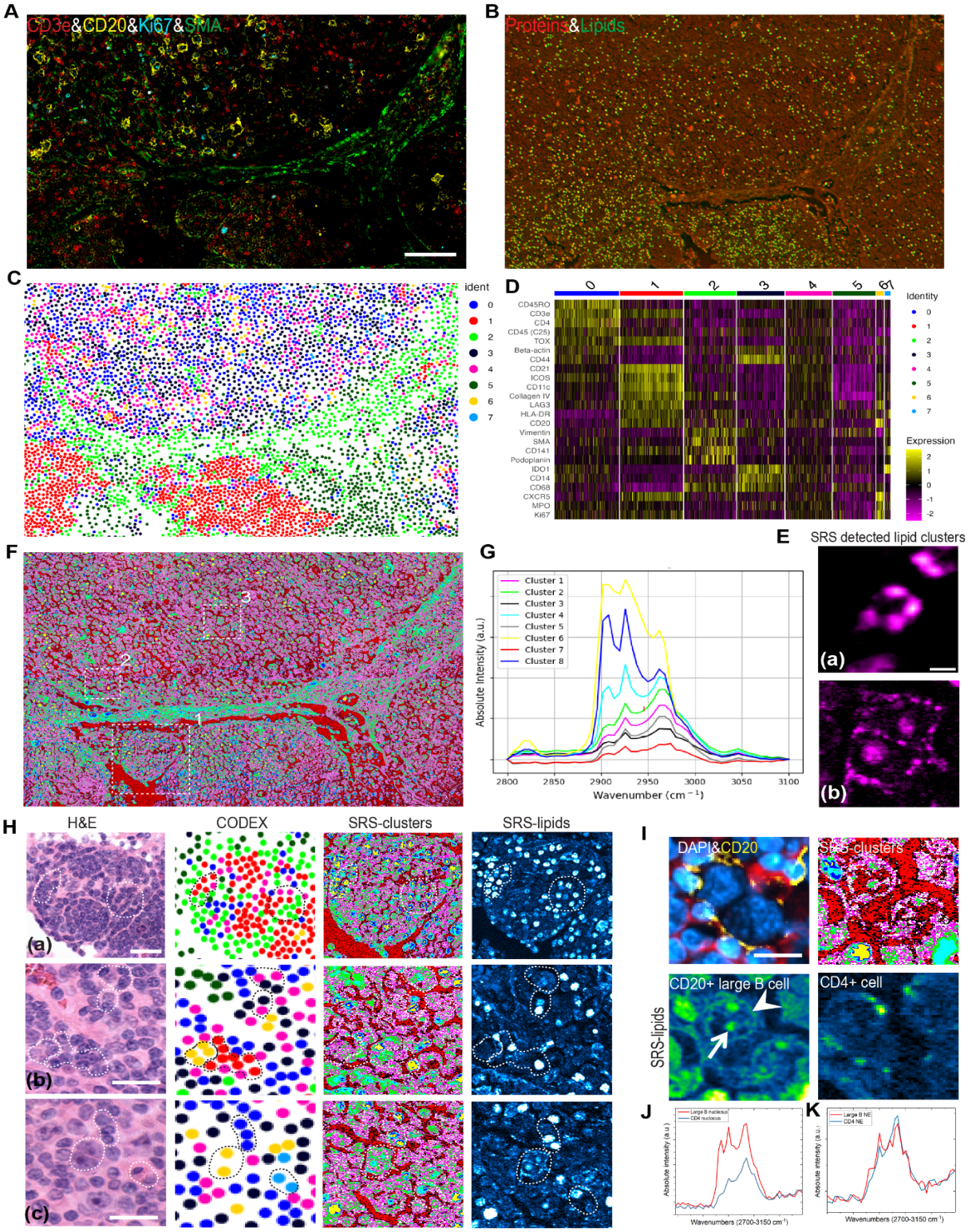

Figure 4. Hyperspectral REDCAT profiles lipid diversity in human lymphoma transformation. (A) Selected CODEX markers showing the distribution of large B tumor and T cells in the lymphoma ROI on which hyperspectral imaging was conducted. **(B)** Overlapping SRS image showing the distribution of proteins and lipids in the lymphoma ROI on which hyperspectral imaging was conducted. **(C-D)** Unsupervised clustering of all the pixels-based protein expression profiles identified 8 distinct clusters in the lymphoma tissue. **(E)** High resolution SRS lipid imaging showing the differences of lipid droplet size and distribution between CLL (a) and DLBCL (b) cells. **(F-G)**

Unsupervised K-means clustering of all the pixels-based SRS hyperspectral images in the lymphoma tissue. **(H)** Spatial co-registration of SRS hyperspectral clusters and CODEX clusters revealing cell type specific metabolic profile. (a) Zoomed in ROI (1) located at CLL region in (F). (b) Zoomed in ROI (2) located at the adjacent region between CLL and DLBCL in (F). (c) Zoomed in ROI (3) located at DLBCL region in (F). **(I)** High resolution SRS lipid imaging showing nucleolus and nuclear envelope localized lipids in large B tumor cell. **(J-K)** SRS hyperspectral imaging revealing the lipid profiles in the subcellar compartments such as nucleolus, nuclear envelope and lipid droplets of large B tumor cell and normal CD4 cell.

Supplementary Figures

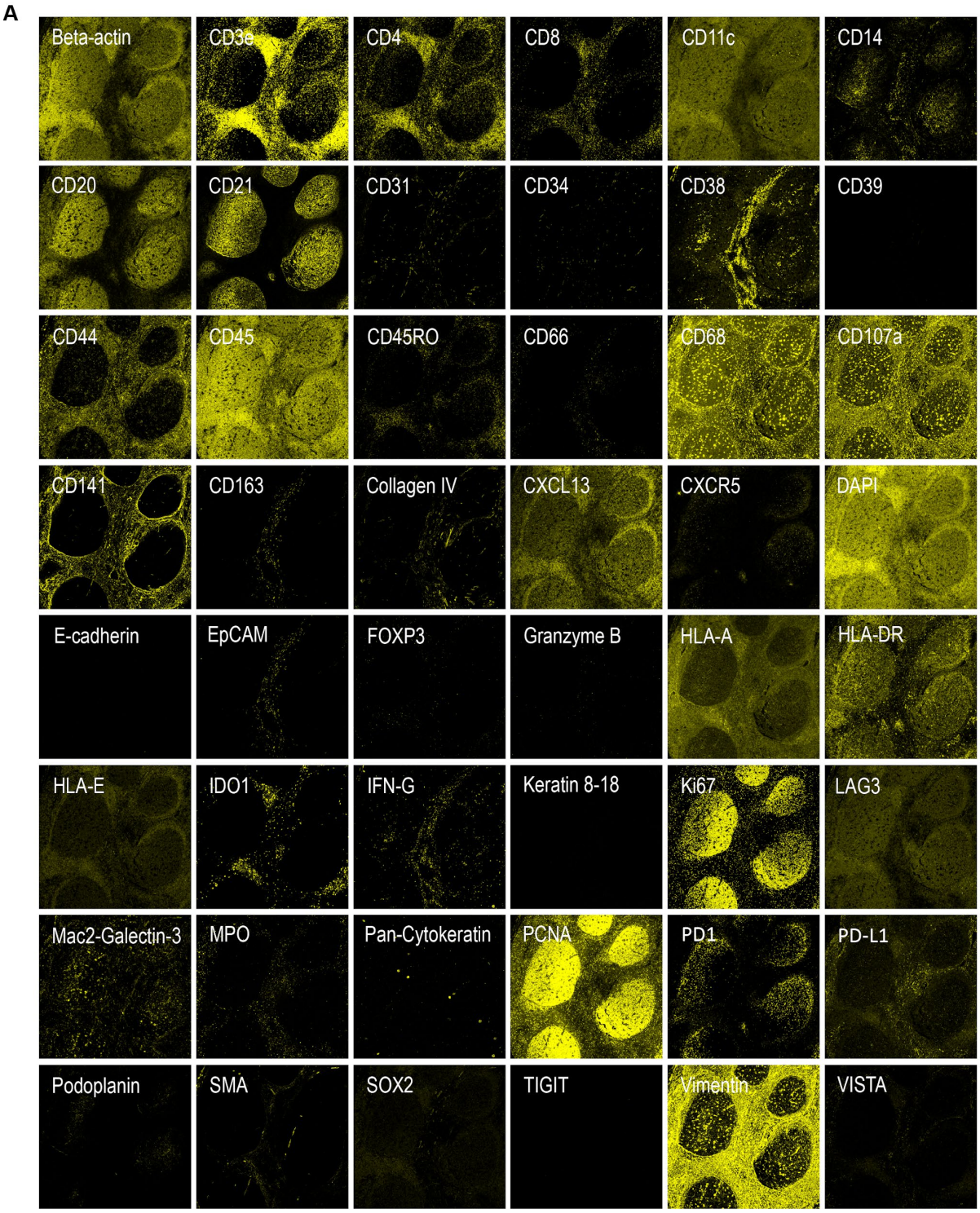

Figure S1. The holistic set of CODEX markers for the normal lymph node

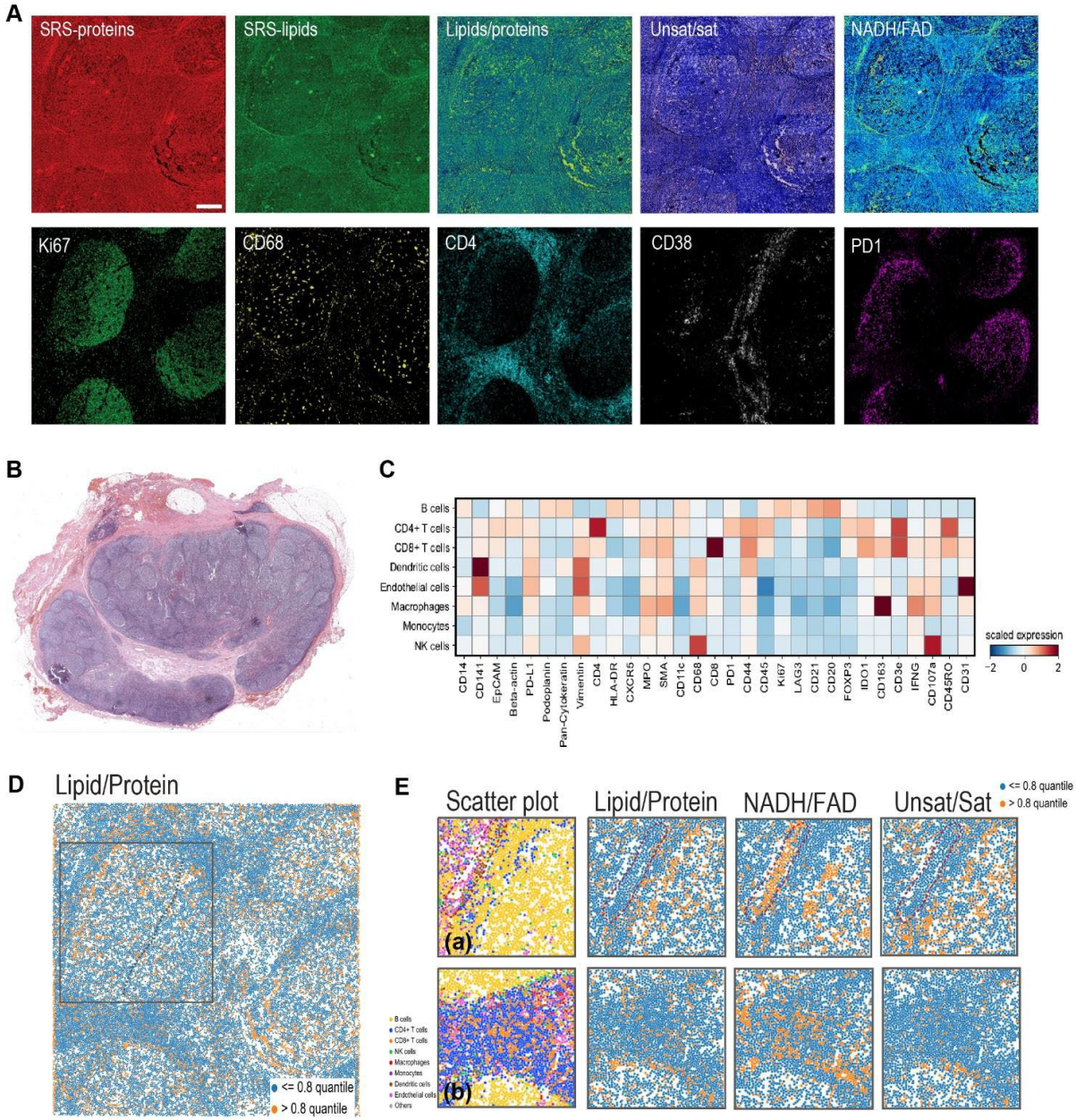

Figure S2. REDCAT profiles the metabolic state in a normal lymph node tissue. (A) TPEF-SRS and selected CODEX panels showing the co-registration of metabolites and proteomics at the same region of interest in the normal lymph nodes. Scale bar: 200 µm. **(B)** H&E image showing the histology of the normal lymph node. **(C)** Matrixplot for mean CODEX expression in each cell type. **(D)** The plot showing single cell lipid level. The ROI inside the black box indicates a typical follicle with a light zone and dark zone, which are separated by a dashed line. **(E)** Zoomed in scatter plots showing single cell lipid level, redox ratio and unsaturated lipid level of ROI a and b indicated in Figure 2G.

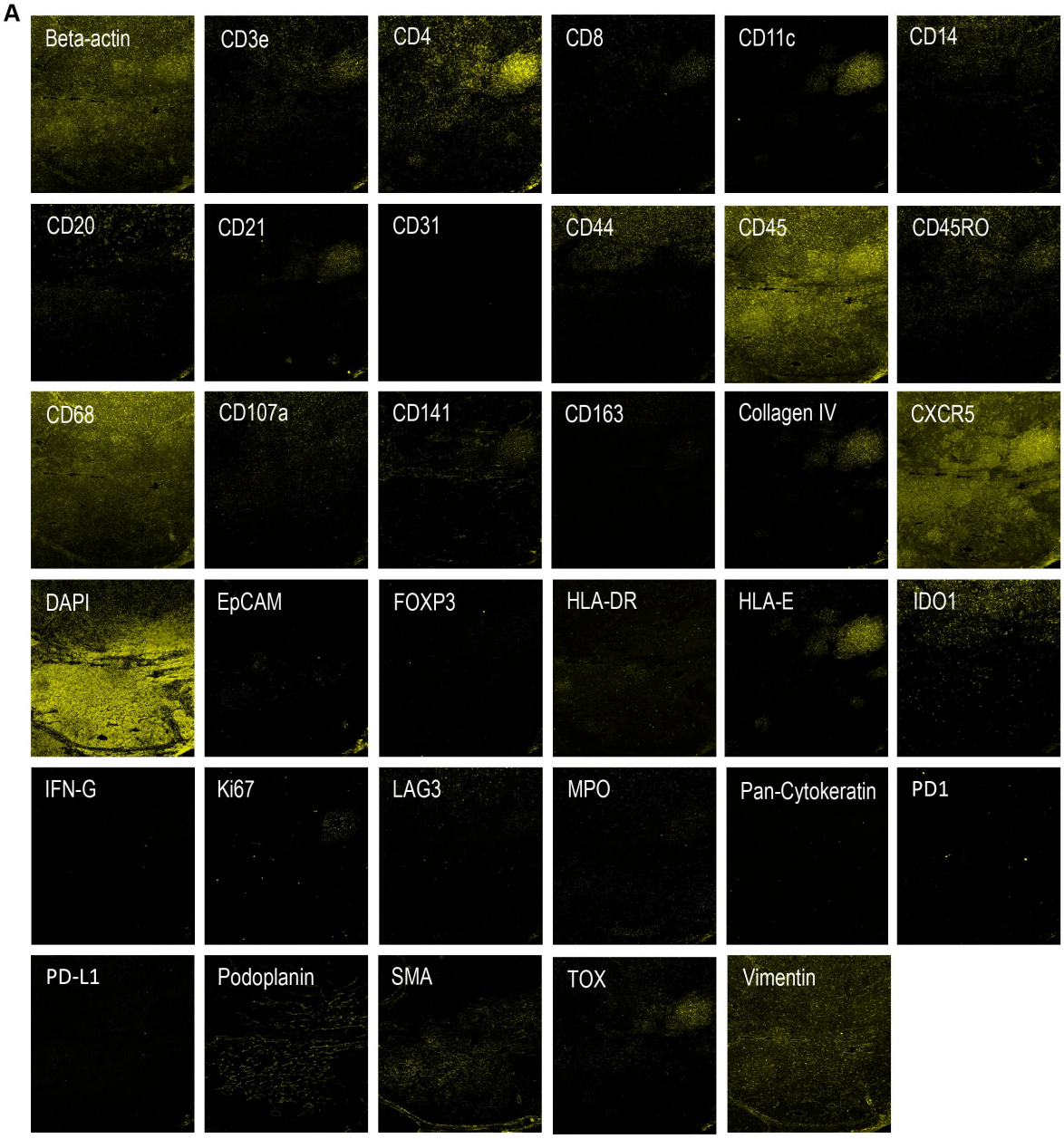

Figure S3. The holistic set of CODEX panels for the lymphoma ROI 1

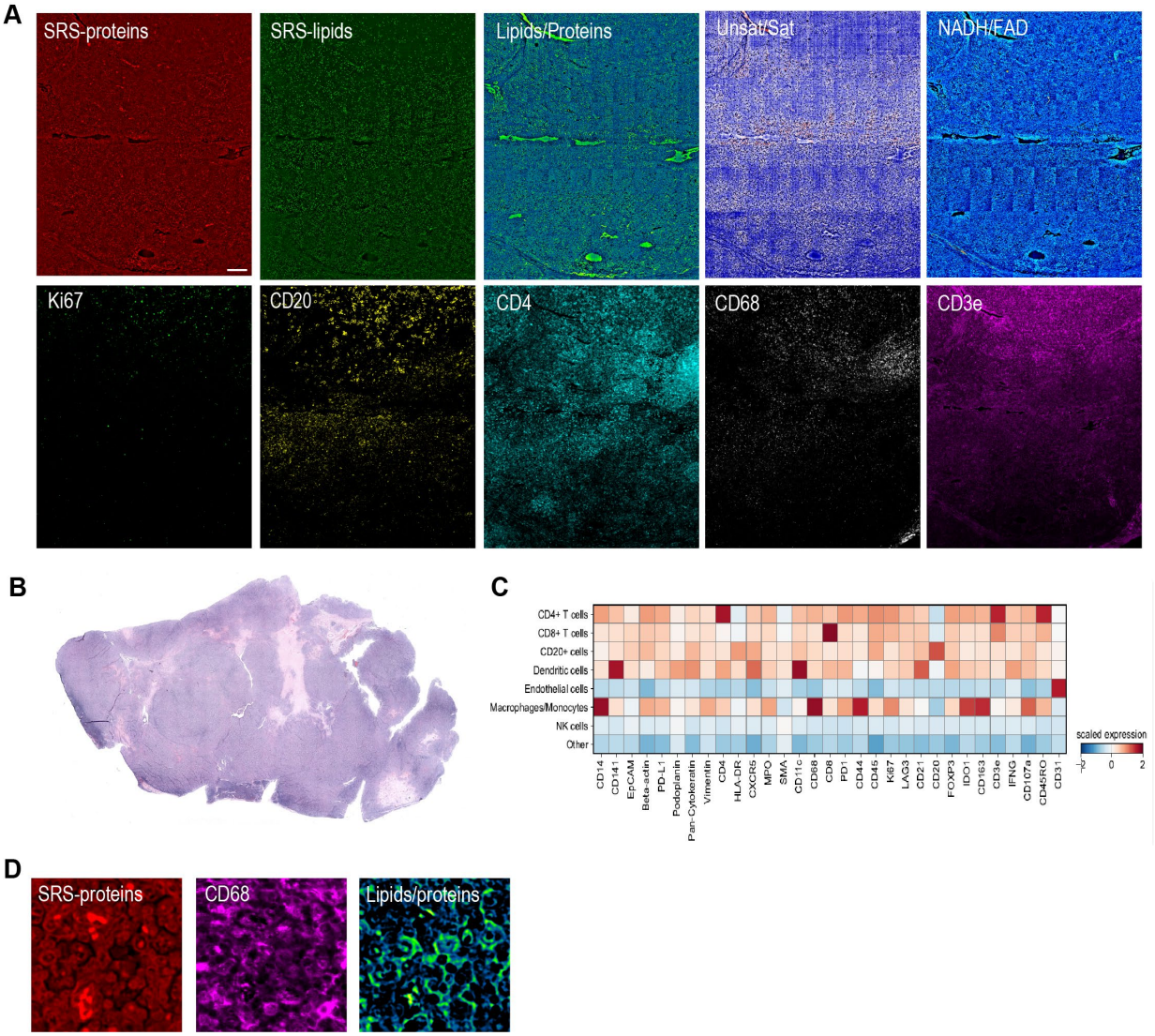

Figure S4. REDCAT profiles the metabolic state in the lymphoma. (A) TPEF-SRS and selected CODEX panels showing the co-registration of metabolites and proteomics at the same region of interest in the lymphoma. Scale bar: 200 µm. **(B)** H&E image showing the histology of the lymphoma tissue. **(C)** Matrixplot for mean expression in each cell type. **(D)** Zoomed in SRS images showing the distribution of lipids in CD68 positive macrophage.

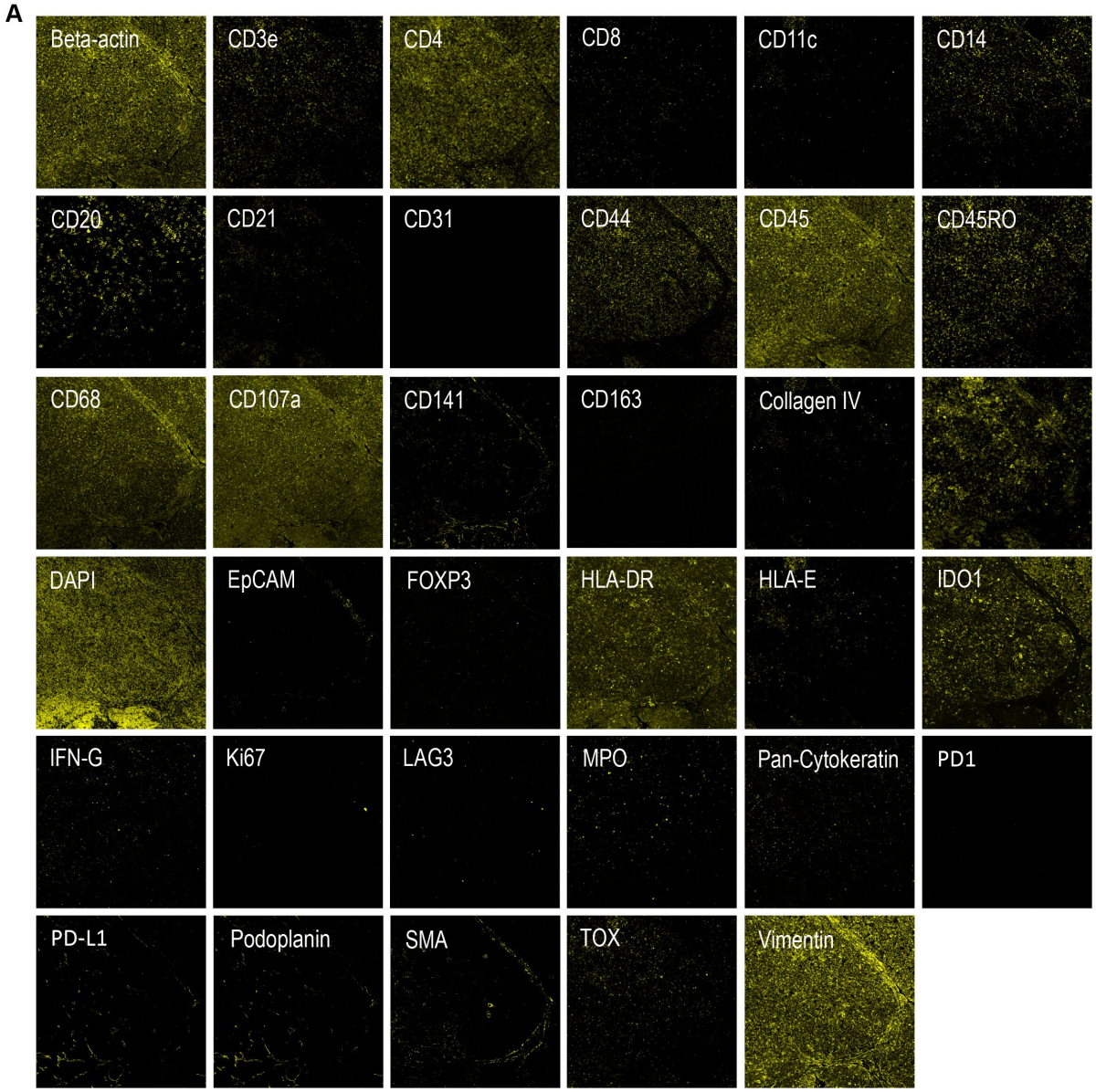

Figure S5. The holistic set of CODEX markers for the lymphoma ROI 2

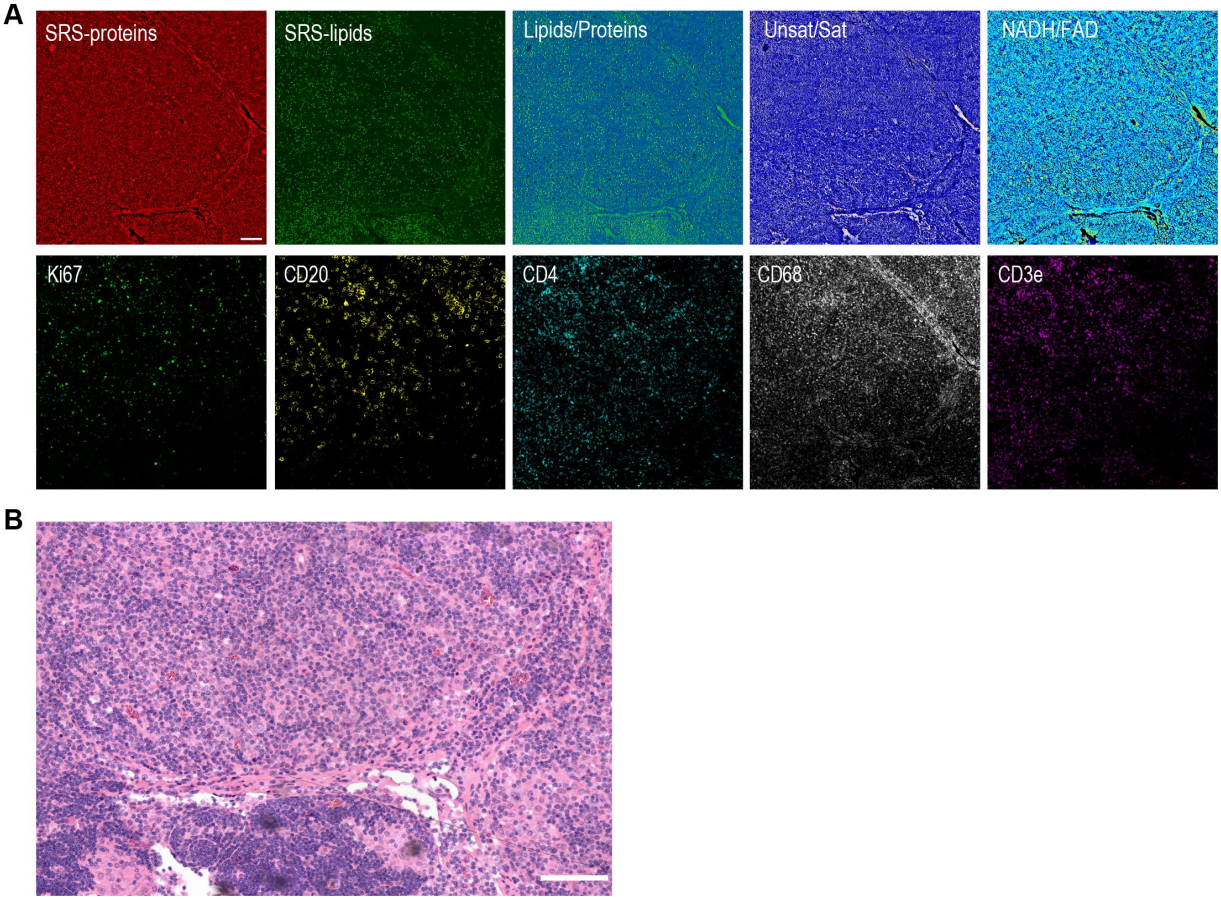

Figure S6. REDCAT profiles the lipid diversity in the lymphoma. (A) TPEF-SRS and selected CODEX panels showing the co-registration of metabolites and proteomics at the same region of interest in the lymphoma. Scale bar: 200 µm. **(B)** H&E image showing the histology of the lymphoma ROI where SRS hyperspectral imaging was performed. Scale bar: 200 µm.

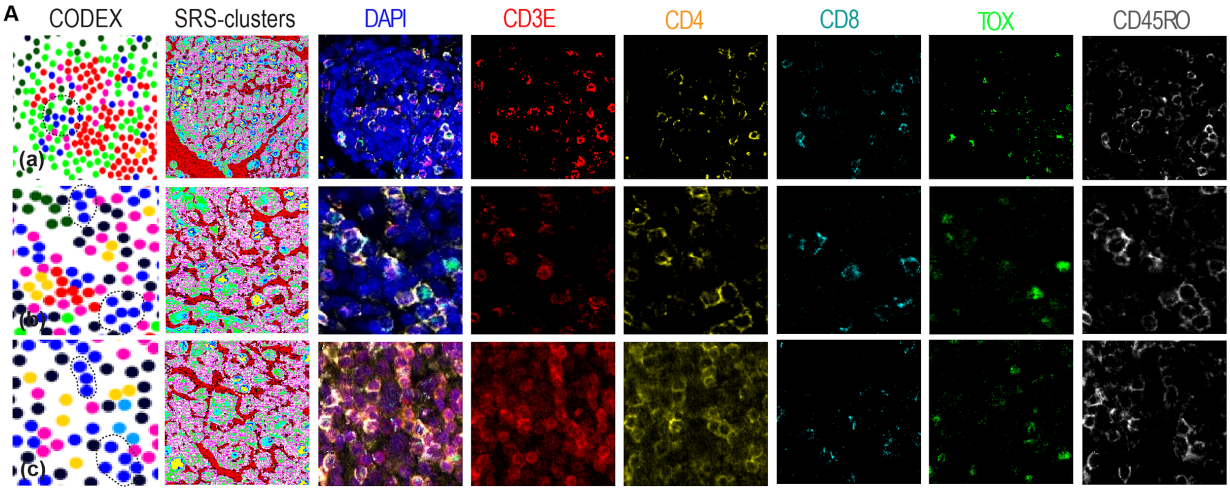

Figure S7. REDCAT profiles metabolic profiles in T cells. Spatial co-registration of SRS hyperspectral clusters and CODEX clusters revealing T cell type specific metabolic profile. (a, b, c) Zoomed in images shown as ROI (1, 2, 3) in Figure 4F.

References

1 Ghosh-Choudhary, S., Liu, J. & Finkel, T. Metabolic Regulation of Cell Fate and Function. *Trends Cell Biol* **30**, 201-212, doi:10.1016/j.tcb.2019.12.005 (2020).

2 Metallo, C. M. & Vander Heiden, M. G. Understanding metabolic regulation and its influence on cell physiology. *Mol Cell* **49**, 388-398, doi:10.1016/j.molcel.2013.01.018 (2013).

3 Sieber, M. H. & Spradling, A. C. The role of metabolic states in development and disease. *Curr Opin Genet Dev* **45**, 58-68, doi:10.1016/j.gde.2017.03.002 (2017).

4 Ståhl, P. L. *et al.* Visualization and analysis of gene expression in tissue sections by spatial transcriptomics. *Science* **353**, 78-82, doi:doi:10.1126/science.aaf2403 (2016).

5 Eng, C. L. *et al.* Transcriptome-scale super-resolved imaging in tissues by RNA seqFISH. *Nature* **568**, 235-239, doi:10.1038/s41586-019-1049-y (2019).

6 Rodriques, S. G. *et al.* Slide-seq: A scalable technology for measuring genome-wide expression at high spatial resolution. *Science* **363**, 1463-1467, doi:doi:10.1126/science.aaw1219 (2019).

7 Liu, Y. *et al.* High-plex protein and whole transcriptome co-mapping at cellular resolution with spatial CITE-seq. *Nat Biotechnol* **41**, 1405-1409, doi:10.1038/s41587-023-01676-0 (2023).

8 Liu, Y. *et al.* High-Spatial-Resolution Multi-Omics Sequencing via Deterministic Barcoding in Tissue. *Cell* **183**, 1665-1681 e1618, doi:10.1016/j.cell.2020.10.026 (2020).

9 Goltsev, Y. *et al.* Deep Profiling of Mouse Splenic Architecture with CODEX Multiplexed Imaging. *Cell* **174**, 968-981 e915, doi:10.1016/j.cell.2018.07.010 (2018).

10 Stoeckius, M. *et al.* Simultaneous epitope and transcriptome measurement in single cells. *Nat Methods* **14**, 865-868, doi:10.1038/nmeth.4380 (2017).

11 Rappez, L. *et al.* SpaceM reveals metabolic states of single cells. *Nat Methods* **18**, 799-805, doi:10.1038/s41592-021-01198-0 (2021).

12 Ganesh, S. *et al.* Spatially resolved 3D metabolomic profiling in tissues. *Science Advances* **7**, eabd0957, doi:doi:10.1126/sciadv.abd0957 (2021).

13 Hu, T. *et al*. Single-cell spatial metabolomics with cell-type specific protein profiling for tissue systems biology. Nat Commun 14, 8260, doi:10.1038/s41467-023-43917-5 (2023).

14 Shi, L. *et al.* Optical imaging of metabolic dynamics in animals. *Nat Commun* **9**, 2995, doi:10.1038/s41467-018-05401-3 (2018).

15 Zhang, W. *et al.* Multi-molecular hyperspectral PRM-SRS microscopy. *Nat Commun* **15**, 1599, doi:10.1038/s41467-024-45576-6 (2024).

16 Jang, H. *et al.* Super-resolution SRS microscopy with A-PoD. *Nat Methods* **20**, 448-458, doi:10.1038/s41592-023-01779-1 (2023).

17 Farmer, B. C., Walsh, A. E., Kluemper, J. C. & Johnson, L. A. Lipid Droplets in Neurodegenerative Disorders. *Front Neurosci* **14**, 742, doi:10.3389/fnins.2020.00742 (2020).

18 Zadoorian, A., Du, X. & Yang, H. Lipid droplet biogenesis and functions in health and disease. *Nat Rev Endocrinol* **19**, 443-459, doi:10.1038/s41574-023-00845-0 (2023).

19 Walther, T. C. & Farese, R. V., Jr. Lipid droplets and cellular lipid metabolism. *Annu Rev Biochem* **81**, 687-714, doi:10.1146/annurev-biochem-061009-102430 (2012).

20 Bailey, A. P. *et al.* Antioxidant Role for Lipid Droplets in a Stem Cell Niche of Drosophila. *Cell* **163**, 340-353, doi:10.1016/j.cell.2015.09.020 (2015).

21 Monson, E. A., Trenerry, A. M., Laws, J. L., Mackenzie, J. M. & Helbig, K. J. Lipid droplets and lipid mediators in viral infection and immunity. *FEMS Microbiol Rev* **45**, doi:10.1093/femsre/fuaa066 (2021).

22 Takahashi, H., Yanamisawa, A., Kajimoto, S. & Nakabayashi, T. Observation of the changes in the chemical composition of lipid droplets using Raman microscopy. *Phys Chem Chem Phys* **22**, 21646-21650, doi:10.1039/d0cp03805a (2020).
23 Thiam, A. R. & Beller, M. The why, when and how of lipid droplet diversity. *J Cell Sci* **130**, 315-324, doi:10.1242/jcs.192021 (2017).
24 Jia, H. & Yue, S. Stimulated Raman Scattering Imaging Sheds New Light on Lipid Droplet Biology. *The Journal of Physical Chemistry B* **127**, 2381-2394, doi:10.1021/acs.jpcb.3c00038 (2023).
25 Heikal, A. A. Intracellular Coenzymes as Natural Biomarkers for Metabolic Activities and Mitochondrial Anomalies. *Biomarkers in Medicine* **4**, 241-263, doi:10.2217/bmm.10.1 (2010).
26 Chance, B., Cohen, P., Jobsis, F. & Schoener, B. Intracellular Oxidation-Reduction States in Vivo. *Science* **137**, 499-508, doi:doi:10.1126/science.137.3529.499 (1962).
27 Ostrander, J. H. *et al.* Optical redox ratio differentiates breast cancer cell lines based on estrogen receptor status. *Cancer Res* **70**, 4759-4766, doi:10.1158/0008-5472.CAN-09-2572 (2010).
28 Alhallak, K., Rebello, L. G., Muldoon, T. J., Quinn, K. P. & Rajaram, N. Optical redox ratio identifies metastatic potential-dependent changes in breast cancer cell metabolism. *Biomed Opt Express* **7**, 4364-4374, doi:10.1364/BOE.7.004364 (2016).
29 Yuan, X. *et al.* NAD(+)/NADH redox alterations reconfigure metabolism and rejuvenate senescent human mesenchymal stem cells in vitro. *Commun Biol* **3**, 774, doi:10.1038/s42003-020-01514-y (2020).
30 Li, Y. *et al.* Microglial lipid droplet accumulation in tauopathy brain is regulated by neuronal AMPK. *Cell Metab*, doi:10.1016/j.cmet.2024.03.014 (2024).
31 Ganeshan, K. & Chawla, A. Metabolic regulation of immune responses. *Annu Rev Immunol* **32**, 609-634, doi:10.1146/annurev-immunol-032713-120236 (2014).
32 Chi, H. Immunometabolism at the intersection of metabolic signaling, cell fate, and systems immunology. *Cell Mol Immunol* **19**, 299-302, doi:10.1038/s41423-022-00840-x (2022).
33 Choi, S. C. & Morel, L. Immune metabolism regulation of the germinal center response. *Exp Mol Med* **52**, 348-355, doi:10.1038/s12276-020-0392-2 (2020).
34 Weisel, F. J. *et al.* Germinal center B cells selectively oxidize fatty acids for energy while conducting minimal glycolysis. *Nat Immunol* **21**, 331-342, doi:10.1038/s41590-020-0598-4 (2020).
35 Gray, E. E. & Cyster, J. G. Lymph node macrophages. *J Innate Immun* **4**, 424-436, doi:10.1159/000337007 (2012).
36 Haka, A. S. *et al.* Exocytosis of macrophage lysosomes leads to digestion of apoptotic adipocytes and foam cell formation. *J Lipid Res* **57**, 980-992, doi:10.1194/jlr.M064089 (2016).
37 Streich, K. *et al.* Dietary lipids accumulate in macrophages and stromal cells and change the microarchitecture of mesenteric lymph nodes. *J Adv Res* **24**, 291-300, doi:10.1016/j.jare.2020.04.020 (2020).
38 Ward, C. *et al.* Autophagy, lipophagy and lysosomal lipid storage disorders. *Biochim Biophys Acta* **1861**, 269-284, doi:10.1016/j.bbalip.2016.01.006 (2016).
39 Demicco, M., Liu, X. Z., Leithner, K. & Fendt, S. M. Metabolic heterogeneity in cancer. *Nat Metab* **6**, 18-38, doi:10.1038/s42255-023-00963-z (2024).
40 Martínez-Reyes, I. & Chandel, N. S. Cancer metabolism: looking forward. *Nature Reviews Cancer* **21**, 669-680, doi:10.1038/s41568-021-00378-6 (2021).
41 Fei, F. *et al.* Plasma Metabolites Forecast Occurrence and Prognosis for Patients With Diffuse Large B-Cell Lymphoma. *Front Oncol* **12**, 894891, doi:10.3389/fonc.2022.894891 (2022).

42 Pang, Y., Lu, T., Xu-Monette, Z. Y. & Young, K. H. Metabolic Reprogramming and Potential Therapeutic Targets in Lymphoma. *Int J Mol Sci* **24**, doi:10.3390/ijms24065493 (2023).
43 Thurgood, L. A. *et al.* Chronic Lymphocytic Leukaemia Relies on Lipid Scavenging and Synthesis As an Energy Source. *Blood* **132**, 3117-3117, doi:10.1182/blood-2018-99-120241 (2018).
44 Toledo, B. *et al.* Deciphering the performance of macrophages in tumour microenvironment: a call for precision immunotherapy. *J Hematol Oncol* **17**, 44, doi:10.1186/s13045-024-01559-0 (2024).
45 Uziel, O. *et al.* CLL-Derived Exosomes Educate Endothelial Cells to Become CLL-Supportive Cells. *Blood* **136**, 11-12, doi:10.1182/blood-2020-141828 (2020).
46 Wu, J. *et al.* PHA-4/FoxA senses nucleolar stress to regulate lipid accumulation in Caenorhabditis elegans. *Nat Commun* **9**, 1195, doi:10.1038/s41467-018-03531-2 (2018).
47 Cave, C. F. & Gahan, P. B. A Cytochemical and Autoradiographic Investigation of Nucleolar Phospholipids. *Caryologia* **23**, 303-312, doi:10.1080/00087114.1970.10796371 (1970).
48 Romanauska, A. & Kohler, A. Lipid saturation controls nuclear envelope function. *Nat Cell Biol* **25**, 1290-1302, doi:10.1038/s41556-023-01207-8 (2023).
49 Bai, Z. *et al.* Spatially exploring RNA biology in archival formalin-fixed paraffin-embedded tissues. *Cell*, doi:10.1016/j.cell.2024.09.001 (2024).
50 Schmidt, U., Weigert, M., Broaddus, C. & Myers, G. in *Medical Image Computing and Computer Assisted Intervention – MICCAI 2018: 21st International Conference, Granada, Spain, September 16-20, 2018, Proceedings, Part II* 265–273 (Springer-Verlag, Granada, Spain, 2018).
51 Bankhead, P. *et al.* QuPath: Open source software for digital pathology image analysis. *Sci Rep* **7**, 16878, doi:10.1038/s41598-017-17204-5 (2017).
52 Greenwald, N. F. *et al.* Whole-cell segmentation of tissue images with human-level performance using large-scale data annotation and deep learning. *Nat Biotechnol* **40**, 555-565, doi:10.1038/s41587-021-01094-0 (2022).
53 Geuenich, M. J. *et al.* Automated assignment of cell identity from single-cell multiplexed imaging and proteomic data. *Cell Syst* **12**, 1173-1186 e1175, doi:10.1016/j.cels.2021.08.012 (2021).